Journal of
Marine Science and Engineering

MDPI

Article

A Time-Domain Wavenumber Integration Model for Underwater Acoustics Based on the High-Order Finite Difference Method

Xiang Xu, Wei Liu * and Guojun Xu *

College of Meteorology and Oceanography, National University of Defense Technology, Changsha 410073, China; xuxiang26@nudt.edu.cn
* Correspondence: liuwei@nudt.edu.cn (W.L.); xuguojun@nudt.edu.cn (G.X.)

Abstract: Simulating the acoustic field excited by pulse sound sources holds significant practical value in computational ocean acoustics. Two primary methods exist for modeling underwater acoustic propagation in the time domain: the Fourier synthesis technique based on frequency decomposition and the time-domain underwater acoustic propagation model (TD-UAPM). TD-UAPMs solve the wave equation in the time domain without requiring frequency decomposition, providing a more intuitive explanation of the physical process of sound energy propagation over time. However, time-stepping numerical methods can accumulate numerical errors, making it crucial to improve the algorithm's accuracy for TD-UAPMs. Herein, the time-domain wavenumber integration model SPARC was improved by replacing the second-order finite element method (FEM) with the high-order accuracy finite difference method (FDM). Furthermore, the matched interface and boundary (MIB) method was used to process the seabed more accurately. The improved model was validated using three classic underwater acoustic benchmarks. By comparing the acoustic solutions obtained using the FDM and the FEM, it is evident that the improved model requires fewer grid points while maintaining the same level of accuracy, leading to lower computational costs and faster processing compared to the original model.

Keywords: wave equation; underwater acoustic propagation; depth-separated wave equation; matched interface and boundary method (MIB)

Citation: Xu, X.; Liu, W.; Xu, G. A Time-Domain Wavenumber Integration Model for Underwater Acoustics Based on the High-Order Finite Difference Method. *J. Mar. Sci. Eng.* **2024**, *12*, 728. https://doi.org/10.3390/jmse12050728

Academic Editor: Rouseff Daniel

Received: 30 March 2024
Revised: 19 April 2024
Accepted: 26 April 2024
Published: 27 April 2024

1. Introduction

The study of underwater acoustic propagation in the time domain has long been a popular topic, especially concerning transient acoustic fields generated by impulsive sources such as underwater explosions and airguns. Jensen et al. [1,2] presented commonly employed models of continuous wave (CW) and impulse propagation, illustrating the efficacy of both acoustic models in accurately characterizing sound propagation within marine environments. In general, the computational effort for a transient sound field is several orders of magnitude higher than that for a single-frequency continuous wave sound field [3], so the development of underwater acoustic time-domain modeling has been relatively slow; however, with the continuous improvement of computer performance, the development of efficient underwater acoustic time-domain models has been increasingly emphasized by underwater acousticians [4]. Two primary approaches exist for modeling underwater acoustic propagation in the time domain: the Fourier synthesis technique (FST) based on frequency decomposition and the time-domain underwater acoustic propagation model (TD-UAPM). Both of these approaches are outlined in the subsequent paragraphs.

The FST calculates the transient acoustic field by performing the Fourier inverse transform of the time-harmonic acoustic field results at multiple frequency points. This approach requires minimal programming effort, and any time-harmonic acoustic models can be linked up with a pulse post-processor, which performs the numerical Fourier synthesis based on some single-frequency calculations within the frequency band of the

sound source [5]. The time-harmonic models comprise ray models [6], normal mode models [7], fast field models [8], and parabolic equation models [9,10], which have been extensively studied. There have been some attempts at this Fourier synthesis technique. Zingarelli et al. [11] proposed an optimized Fourier synthesis technique to improve the efficiency of calculating individual frequency components and avoid unnecessary frequency runs. Deavenport et al. [12] proposed a technique to perform the convolution operation of the source signal with the medium's impulse response directly in the time domain, which can more accurately model the propagating band-limited transient signals in underwater acoustics in comparison with the traditional Fourier synthesis method. An et al. [13] proposed an optimized Fourier synthesis method to accelerate the modeling of the impulse response function.

Although the FSTs are capable of fast synthesis using existing time-harmonic models, they may not accurately handle rapid signal changes in transient acoustic fields. In contrast, the TD-UAPM solves the wave equation with any given signal function without requiring frequency decomposition and provides a more intuitive explanation of the physical process of transient acoustic propagation. However, new TD-UAPM codes need to be developed. In 1985, Murphy [14] introduced a practical numerical simulation framework for studying underwater sound propagation by introducing the time-domain parabolic wave equation and the finite difference method (FDM). This approach can consider the discontinuities in the acoustic velocity and the density, and can obtain the numerical solution by solving the system of tridiagonal linear equations. Collins [15] developed a wide-angle time-domain parabolic equation model, which was numerically solved and verified. Özkan [16] proposed a time-domain normal mode solution for single-layer acoustic waveguides in Cartesian coordinates. Cristini et al. [17] utilized the spectral element method to present numerical results in the time domain, providing a robust approach for computing wavefields in the ocean.

The wavenumber integration model (also named the fast field program) [18,19] provides a reliable and efficient simulation method for describing acoustic wave propagation by applying the Hankel transform to a stratified medium. Porter [20] proposed a time-marched fast field program called SPARC, and the Hankel transform was used to convert the horizontal distance to the horizontal wavenumber, which converts the original partial differential equation into a set of ordinary differential equations in depth coordinates (also known as depth equations). The finite element method (FEM) [21] was then used to directly solve the depth equation for the partial pressure field corresponding to each horizontal wavenumber, followed by the Hankel inverse transform to obtain the transient acoustic pressure field. However, time-stepping numerical methods may accumulate numerical errors, so it is critical to improve the accuracy of the TD-UAPM algorithm. This study improves the SPARC by replacing the second-order finite element method with a high-order accuracy FDM. In addition, the seabed is treated more accurately by utilizing the matched interface and boundary method (MIB) [22,23]. Furthermore, the improved model was validated by using three classical underwater acoustic benchmarks. The proposed fourth-order FDM in this model requires fewer grid points compared to the original SPARC program, which utilizes the second-order FEM. Despite the reduction in grid points, the improved program maintains or even surpasses the level of accuracy in the original, resulting in decreased computational costs and faster processing times.

The structure of this paper is as follows: in Section 2 the time-domain wavenumber integration model is introduced; Section 3 discusses the high-order FDM for solving the depth equation; Section 5 presents three transient acoustic test cases; and Section 5 summarizes the entire paper.

2. Time-Domain Wavenumber Integration Model

The wave equation for a Cartesian coordinate system in the time domain, accounting for medium absorption, can be expressed as [20]:

$$\left(1+d(z)\frac{\partial}{\partial t}\right)\left[\rho(z)\nabla\cdot\left(\frac{1}{\rho(z)}\nabla p\right)\right]-\frac{1}{c^2(z)}\frac{\partial^2 p}{\partial t^2}=-4\pi s(t)\delta(R) \tag{1}$$

where $p(r, z, t)$ represents the acoustic pressure as a function of the depth z, horizontal distance r, and time t. The terms $s(t)$ and $\delta(R)$ denote an isotropic point source function and the Dirac function dependance on the distance R, respectively. The variables $\rho(z)$, $c(z)$, and $d(z)$ represent the density, sound speed, and attenuation of the medium, respectively.

2.1. Hankel Transform of the Wave Equation

In a horizontally stratified marine environment, the sound field excited by an omnidirectional point source exhibits axial symmetry and is independent of the circumferential direction in a cylindrical coordinate system; thus, the Equation (1) is transformed into cylindrical coordinates, which can be expressed as follows [24]:

$$\left(1+d(z)\frac{\partial}{\partial t}\right)\left[\frac{\rho}{r}\frac{\partial}{\partial r}\left(\frac{r}{\rho}\frac{\partial p}{\partial r}\right)+\rho\frac{\partial}{\partial z}\left(\frac{1}{\rho}\frac{\partial p}{\partial z}\right)\right]-\frac{1}{c^2}\frac{\partial^2 p}{\partial t^2}=-4\pi s(t)\frac{\delta(z-z_s)\delta(r)}{2\pi r} \tag{2}$$

where z_s represents the depth of the sound source, the z-axis represents the vertical axis passing through the sound source, and the r-axis is parallel to the sea surface. To eliminate the term $\delta(r)$ on the right-hand side of this equation, the horizontal distance r is converted to a series of horizontal wavenumbers k_r using the Hankel transform. The formulas for the Hankel transform and its inverse transform are as follows:

$$p(r,z,t)=\int_0^\infty \hat{p}(k_r,z,t)J_0(k_r r)k_r dk_r \tag{3}$$

$$\hat{p}(z,t;k_r)=\int_0^\infty p(r,z,t)J_0(k_r r)r dr \tag{4}$$

where $J_0(k_r r)$ is the Bessel function. If both sides of Equation (2) are multiplied by $J_0(k_r r)r$ and then integrated over r, we can obtain the depth-separated wave equation (the depth equation) in the time domain:

$$\left(1+d(z)\frac{\partial}{\partial t}\right)\left[\rho\frac{\partial}{\partial z}\left(\frac{1}{\rho}\frac{\partial \hat{p}}{\partial z}\right)-k_r^2\hat{p}\right]-\frac{1}{c^2}\hat{p}_{tt}=-2s(t)\delta(z-z_s) \tag{5}$$

If a linear operator is defined:

$$\mathcal{L}(\hat{p})=\rho\frac{\partial}{\partial z}\left(\frac{1}{\rho}\frac{\partial \hat{p}}{\partial z}\right)-k_r^2\hat{p} \tag{6}$$

Then, the depth equation can be changed to:

$$\mathcal{L}(\hat{p})+d(z)\mathcal{L}(\hat{p}_t)-c^{-2}\hat{p}_{tt}=-2s(t)\delta(z-z_s) \tag{7}$$

where $\hat{p}_t=\partial\hat{p}/\partial t$ and $\hat{p}_{tt}=\partial^2\hat{p}/\partial t^2$. This equation is a partial differential equation that involves the time evolution at different depths. Therefore, boundary and initial conditions are required to fully determine the problem [25]. The upper and lower boundary conditions of the acoustic field are assumed to be pressure release conditions at $z = 0$ and $z = H$, respectively:

$$\hat{p}(r,0,t)=0,\quad \hat{p}(r,H,t)=0 \tag{8}$$

In addition, assume that the medium is initially at rest,

$$\hat{p}(r,z,0) = \hat{p}_t(r,z,0) = 0 \tag{9}$$

2.2. Wavenumber Discretization

If the depth Equation (7) corresponding to each horizontal wavenumber is solved, the sound pressure field can be obtained by calculating the discretized inverse Hankel transform. First, numerical truncation is applied to the horizontal wavenumbers:

$$p(r,z,t) = \int_0^\infty \hat{p}(z,t;k_r)J_0(k_r r)k_r dk_r \approx \int_{k_{\min}}^{k_{\max}} \hat{p}(z,t;k_r)J_0(k_r r)k_r dk_r \tag{10}$$

where

$$k_{\min} = 2\pi f_{\min}/c_{\max}, k_{\max} = 2\pi f_{\max}/c_{\min} \tag{11}$$

$f_{\min}$ and $f_{\max}$ represent the truncated minimum and maximum frequencies of the sound source, respectively, and this frequency range contains the majority of the sound energy. $c_{\min}$ is the minimum phase velocity, which is typically determined based on the reference sound speed (e.g., 500 m/s for a reference speed of 1500 m/s), and a smaller value for $c_{\min}$ results in more accurate calculations but requires more computational effort. $c_{\max}$ is the maximum phase velocity, usually chosen as a large value (e.g., 10^7) corresponding to $k_{\min} \approx 0$. Further discretization of the horizontal wavenumbers is then performed:

$$k_r \to k_{r,n} = k_{\min} + (n-1)\Delta k_r = n\Delta k_r + k_{\min} - \Delta k_r \tag{12}$$

where n represents the number of wavenumber sampling points, N_k is the number of segments, and $1 \le n \le N_k + 1$. Then, the integral equation for sound pressure with horizontal wavenumbers can be discretized as follows:

$$p(r,z,t) \approx \Delta k_r \sum_{n=1}^{N_k} \hat{p}(z,t;k_{r,n})J_0(k_{r,n}r)k_{r,n} \tag{13}$$

Since the Bessel function can usually be approximated as [3]:

$$J_0(k_{r,n}r) \approx \frac{e^{i(k_{r,n}r-\pi/4)}}{\sqrt{2\pi k_{r,n}r}} = \frac{1}{\sqrt{2\pi k_{r,n}r}}[\cos(k_{r,n}r - \pi/4) + i\sin(k_{r,n}r - \pi/4)] \tag{14}$$

The real and imaginary parts of this function exhibit periodic oscillations with a gradual decrease in amplitude as the value of $k_r r$ increases. Thus, for each fixed r, it is crucial to have a sufficient number of horizontal wavenumber sampling points for $k_r r$ within a 2π period to achieve accurate integration. Let us assume that there are n_R wavenumber sampling points per period, and typically, $n_R \ge 8$. To accurately calculate the pressure at the maximum horizontal distance ($R_{\max}$), the step size of the wavenumber should be given by:

$$\Delta k_r = \frac{2\pi}{n_R R_{\max}} \tag{15}$$

Then, the number of sampling points for the horizontal wavenumber can be calculated as follows (one more than the number of sampling intervals):

$$n = N_k + 1 = \text{int}\left[\frac{k_{\max} - k_{\min}}{\Delta k_r}\right] + 1 = \text{int}\left[\frac{n_R R_{\max}(k_{\max} - k_{\min})}{2\pi}\right] + 1 \tag{16}$$

3. The FDM for Solving the Depth Equation

The depth Equation (7) has to be discretized and solved to obtain the kernel function $\hat{p}$. Herein, we apply second- and fourth-order finite difference schemes for the derivative discretization with respect to time and depth, respectively.

3.1. Temporal Discretization

To discretize the temporal derivative, kernel functions are used at different time steps. Let superscripts "$(n-1)$", "(n)", and "$(n+1)$" represent the previous, current, and next (unknown) time steps, respectively. Then, second-order accuracy finite difference schemes for first and second temporal derivatives can be, respectively, obtained from Taylor's formulas:

$$\frac{\partial p^{(n)}}{\partial t} = \frac{\hat{p}^{(n+1)} - \hat{p}^{(n-1)}}{2\Delta t} + O\left[(\Delta t)^2\right] \tag{17}$$

$$\frac{\partial^2 \hat{p}^{(n)}}{\partial t^2} = \frac{\hat{p}^{(n+1)} - 2\hat{p}^{(n)} + \hat{p}^{(n-1)}}{(\Delta t)^2} + O\left[(\Delta t)^2\right] \tag{18}$$

Thus, Equation (7) can be reduced to:

$$\mathcal{L}\left(\hat{p}^{(n)}\right) + d(z)\mathcal{L}\left(\frac{\hat{p}^{(n+1)} - \hat{p}^{(n-1)}}{2\Delta t}\right) - \frac{\hat{p}^{(n+1)} - 2\hat{p}^{(n)} + \hat{p}^{(n-1)}}{(c\Delta t)^2} = -2s(n\Delta t)\delta(z - z_s) \tag{19}$$

Expanding the second term on the left-hand side of this equation linearly results in:

$$\frac{d(z)}{2\Delta t}\mathcal{L}\left(\hat{p}^{(n+1)}\right) - \frac{\hat{p}^{(n+1)}}{(c\Delta t)^2} = RHS \tag{20}$$

where *RHS* (right-hand side) is

$$RHS = -2s(n\Delta t)\delta(z - z_s) + \frac{\hat{p}^{(n-1)} - 2\hat{p}^{(n)}}{(c\Delta t)^2} + \frac{d(z)}{2\Delta t}\mathcal{L}\left(\hat{p}^{(n-1)}\right) - \mathcal{L}\left(\hat{p}^{(n)}\right) \tag{21}$$

where the term "$\mathcal{L}\left(\hat{p}^{(n-1)}\right)$" can be directly taken as the "$\mathcal{L}\left(\hat{p}^{(n)}\right)$" value from the previous time step. To simplify this equation, in the following paragraph, the superscript "(n)" may be removed from variables at the current time step, denoted as $\hat{p}^{(n)} \to \hat{p}$.

The time step size for an explicit scheme needs to satisfy the following Courant–Friedrichs–Lewy (*CFL*) condition [20] to ensure computational stability:

$$\Delta t = CFL\frac{\sqrt{\Delta z_{\min}^2 + \lambda_{\min}^2}}{c_{\max}} \tag{22}$$

where $0 < CFL < 1$, and the specific value can be determined through numerical experiments (in this study, $CFL = 0.5$). $\Delta z_{\min}$ is the minimum depth step size, and $\lambda_{\min}$ is the minimum wavelength in the sound field (the horizontal step size). To ensure the numerical accuracy of the FDM, it is crucial to have a sufficient number of grid segments per wavelength, also known as points per wavelength (*PPW*), and then the minimum depth step size can be calculated by

$$\Delta z_{\min} = \lambda_{\min}/PPW \tag{23}$$

Thus, Equation (22) can be reduced to (herein, $PPW \geq 15$):

$$\Delta t = \frac{CFL\lambda_{\min}\sqrt{PPW^2 + 1}}{c_{\max}PPW} \approx \frac{CFL\lambda_{\min}}{c_{\max}} \tag{24}$$

3.2. Spatial Discretization

As shown in Figure 1, the marine sound field can be divided into the water layer (Layer 1) and the sediment layer (Layer 2). When the sediment layer is considered infinitely thick, it is necessary to artificially truncate the sediment layer at a sufficient depth and set a pressure release boundary condition at this truncation depth. To mitigate the numerical reflections caused by the artificial truncation, an absorbing layer with larger absorption coefficients is commonly added to the lower part of the sediment layer. Uniformly dis-

tributed grid points within each layer are set to facilitate calculations, and it is ensured that there is a shared grid point (referred to as "*D*") at the interface between the water layer and the sediment layer.

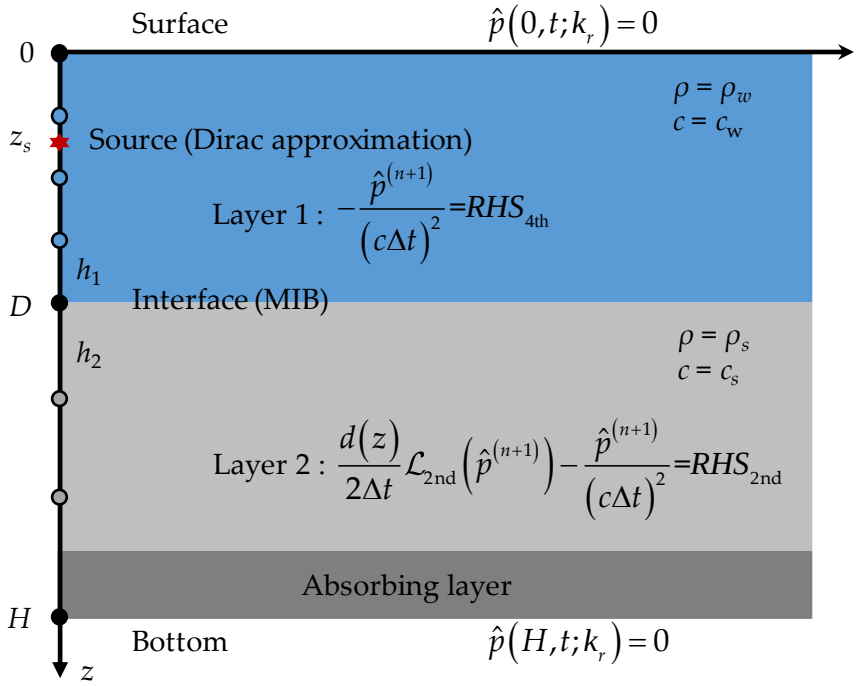

Figure 1. Schematic diagram of the distance-independent marine environment.

Since the water layer contains the source and receiver, thus the sound field within the water layer is usually of interest to us. To enhance the precision of numerical calculations in the water layer, a fourth-order accuracy finite difference scheme has been devised for discretizing the spatial derivatives of the *RHS* in the Equation (20). Furthermore, due to $d(z) = 0$ in water, the Equation (20) can be expressed in a time-marched explicit scheme, given by

$$-\frac{\hat{p}^{(n+1)}}{(c\Delta t)^2} = RHS_{4\text{th}} \tag{25}$$

where

$$RHS_{4\text{th}} = -2s(t)\delta(z-z_s) + \frac{\hat{p}^{(n-1)} - 2\hat{p}^{(n)}}{(c\Delta t)^2} + \frac{d(z)}{2\Delta t}\mathcal{L}_{4\text{th}}\left(\hat{p}^{(n-1)}\right) - \mathcal{L}_{4\text{th}}\left(\hat{p}^{(n)}\right) \tag{26}$$

On the other hand, the primary purpose of calculating the sediment layer is to minimize non-physical reflections on the sound field in the water layer, and artificially increasing the absorption coefficient $d(z)$ in the absorbing layer will also reduce the accuracy of numerical calculations in the sediment layer. Therefore, the second-order spatial differencing scheme is employed in the sediment layer to maintain the tridiagonal property as in the case with the original second-order FEM, and then the Equation (20) can be expressed as

$$\frac{d(z)}{2\Delta t}\mathcal{L}_{2\text{nd}}\left(\hat{p}^{(n+1)}\right) - \frac{\hat{p}^{(n+1)}}{(c\Delta t)^2} = RHS_{2\text{nd}} \tag{27}$$

$$RHS_{2\text{nd}} = -2s(t)\delta(z-z_s) + \frac{\hat{p}^{(n-1)} - 2\hat{p}^{(n)}}{(c\Delta t)^2} + \frac{d(z)}{2\Delta t}\mathcal{L}_{2nd}\left(\hat{p}^{(n-1)}\right) - \mathcal{L}_{2nd}\left(\hat{p}^{(n)}\right) \tag{28}$$

3.2.1. Interior Point Schemes

Since the medium density is generally approximated as a constant within each medium layer, the linear operator can be simplified as follows:

$$\mathcal{L}(\hat{p}) = \frac{\partial}{\partial z}\left(\frac{\partial \hat{p}}{\partial z}\right) - k_r^2 \hat{p} \tag{29}$$

For interior grid points that are far away from the source point, medium interface, and upper/lower boundaries of the acoustic field, the second derivative at an integer index point can be discretized using the first derivatives at adjacent half-integer index points via the FDM with $2(L+1)$th-order accuracy:

$$\left.\frac{\partial}{\partial z}\left(\frac{\partial \hat{p}}{\partial z}\right)\right|_j = \frac{1}{h}\sum_{l=0}^{L} a_l \left[\left(\frac{\partial \hat{p}}{\partial z}\right)_{j+l+1/2} - \left(\frac{\partial \hat{p}}{\partial z}\right)_{j-l-1/2}\right] + O\left(h^{2(L+1)}\right), (L \geq 0) \tag{30}$$

where h represents the grid spacing in the depth direction, j denotes the integer index of the interior grid point, and the coefficient a_l can be calculated using the Taylor expansion and the undetermined coefficient method. Similarly, the first derivative at half-integer index points can be further discretized using the kernel function values at adjacent integer index points:

$$\left(\frac{\partial \hat{p}}{\partial z}\right)_{j+1/2} = \frac{1}{h}\sum_{l=0}^{L} a_l \left(\hat{p}_{j+l+1} - \hat{p}_{j-l-1}\right) + O\left(h^{2(L+1)}\right) \tag{31}$$

Taking $L = 0$, then the second-order accuracy scheme can be obtained:

$$\left.\frac{\partial}{\partial z}\left(\frac{\partial \hat{p}}{\partial z}\right)\right|_j = \frac{1}{h}\left[\left(\frac{\partial \hat{p}}{\partial z}\right)_{j+1/2} - \left(\frac{\partial \hat{p}}{\partial z}\right)_{j-1/2}\right], \left(\frac{\partial \hat{p}}{\partial z}\right)_{j+1/2} = \frac{1}{h}\left(\hat{p}_{j+1} - \hat{p}_j\right) \tag{32}$$

Taking $L = 1$, then the fourth-order accuracy scheme can be obtained:

$$\left.\frac{\partial}{\partial z}\left(\frac{\partial \hat{p}}{\partial z}\right)\right|_j = \frac{1}{24h}\left\{27\left[\left(\frac{\partial \hat{p}}{\partial z}\right)_{j+1/2} - \left(\frac{\partial \hat{p}}{\partial z}\right)_{j-1/2}\right] - \left[\left(\frac{\partial \hat{p}}{\partial z}\right)_{j+3/2} - \left(\frac{\partial \hat{p}}{\partial z}\right)_{j-3/2}\right]\right\} \tag{33}$$

$$\left(\frac{\partial \hat{p}}{\partial z}\right)_{j+1/2} = \frac{1}{24h}\left[27\left(\hat{p}_{j+1} - \hat{p}_j\right) - \left(\hat{p}_{j+2} - \hat{p}_{j-1}\right)\right] \tag{34}$$

It can be observed that the fourth-order accuracy finite difference scheme for calculating the second derivative at point j involves seven grid points ($j-3$, $j-2$, $j-1$, j, $j+1$, $j+2$, and $j+3$). Therefore, special treatment is necessary for the fourth-order finite difference schemes at points near the upper boundary or seabed interface in the water layer. In the sediment layer, the second-order scheme involves only three grid points ($j-1$, j, and $j+1$), and thus the interior point scheme can be used at all grid points in the sediment layer (the interface point belongs to the water layer).

3.2.2. Boundary Schemes

For the upper boundary of the water layer, mark the boundary point as b ($b = 1$), as shown in Figure 2. Due to the pressure release boundary condition, the acoustic pressure at this boundary point is $\hat{p}_b = \hat{p}(z_b, t; k_r) = 0$. In the fourth-order finite difference scheme, the second derivative at the integer index $b+1$ (near the upper boundary) can be given by

$$\begin{aligned}\left.\frac{\partial}{\partial z}\left(\frac{\partial \hat{p}}{\partial z}\right)\right|_{b+1} = \frac{1}{840h}\Bigg[&128\left(\frac{\partial \hat{p}}{\partial z}\right)_b - 1085\left(\frac{\partial \hat{p}}{\partial z}\right)_{b+1/2} \\ &+1015\left(\frac{\partial \hat{p}}{\partial z}\right)_{b+3/2} - 63\left(\frac{\partial \hat{p}}{\partial z}\right)_{b+5/2} + 5\left(\frac{\partial \hat{p}}{\partial z}\right)_{b+7/2}\Bigg]\end{aligned} \tag{35}$$

where the first derivatives at the boundary point and the half-integer index point of $b + 1/2$ can be further expressed as follows:

$$\left(\frac{\partial \hat{p}}{\partial z}\right)_b = \frac{1}{12h}(-25\hat{p}_b + 48\hat{p}_{b+1} - 36\hat{p}_{b+2} + 16\hat{p}_{b+3} - 3\hat{p}_{b+4}) \tag{36}$$

$$\left(\frac{\partial \hat{p}}{\partial z}\right)_{b+1/2} = \frac{1}{24h}(-22\hat{p}_b + 17\hat{p}_{b+1} + 9\hat{p}_{b+2} - 5\hat{p}_{b+3} + \hat{p}_{b+4}) \tag{37}$$

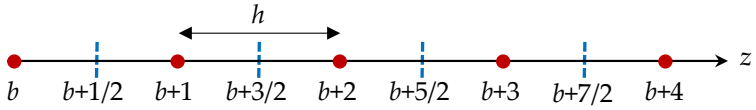

Figure 2. Schematic diagram of point indexes near the upper boundary.

The first derivatives at other half-integer index points in the Equation (35) can be calculated using the interior point schemes from the Equation (34).

3.2.3. Interface Schemes

The FEM used in the original SPARC program divides the entire region into a number of independent cells. The continuity of sound pressure at the interfaces between cells can be ensured by sharing nodes between cells. On the other hand, the condition of continuity of vertical vibration velocity between neighboring cells has been applied as a known condition in the derivation of the FEM schemes. Thus, the acoustic pressure and normal vibration velocity at the seabed interface can be smoothly connected without additional treatment.

However, the FDM can only be applied in regions where the derivatives are continuous at all orders. This presents a challenge when dealing with the seabed interface, as the derivatives of the kernel function are discontinuous on both sides. As a result, special treatment is required. Additionally, the FDM used for the frequency-domain depth equation cannot be directly applied to the time-domain depth equation. This is because the frequency-domain FDM first establishes the first derivative difference equation on each side above and below the interface point. It then replaces the second derivative term in the equation with the kernel function term based on the Helmholtz equation, while ignoring derivatives higher than the third order. By imposing the condition of equal vertical vibration velocity, a relationship equation for the first derivatives on both sides of the interface point is established. This leads to the formation of a relationship equation containing the kernel functions corresponding to the interface point and the upper and lower neighboring points, known as the finite–difference interface processing method for the frequency-domain depth equation. On the other hand, the time-domain depth equation includes time derivative terms of the kernel function, making it impossible to treat the interface conditions as completed in the frequency-domain processing method. To address this issue, this paper draws on the matched interface and boundary method (MIB), commonly used in computational mathematics for dealing with interfaces, and introduces it into the time-domain depth equation, resulting in satisfactory results.

At the interface between different media, the acoustic pressure and the vertical velocity are continuous on both sides. For instance, at the interface between the water and sediment layer located at $z = D$ [25]:

$$\hat{p}(D^-, t; k_r) = \hat{p}(D^+, t; k_r), \frac{1}{\rho_w}\frac{\partial \hat{p}(z, t; k_r)}{\partial z}\bigg|_{z=D^-} = \frac{1}{\rho_s}\frac{\partial \hat{p}(z, t; k_r)}{\partial z}\bigg|_{z=D^+} \tag{38}$$

Different media layers may require different grid steps due to variations in the sound speed and wavelength for the same frequency. If the neighboring media layers have different grid steps in the depth direction, the media interface needs to be arranged on a specific grid point, and the acoustic pressure value at this interface point is shared by the

two media layers. Herein, the sound pressure at the interface point is calculated using the matched interface and boundary method.

The index of the interface point is denoted as j. Medium A (with grid spacing h_A) is located above the interface, while medium B (with grid spacing h_B) is located below it. The acoustic pressure is extended smoothly and continuously from points above j to a virtual point J+1, located at a distance of h_A from point j. Suppose the acoustic pressure value at this virtual point is q_{J+1}, as shown in Figure 3.

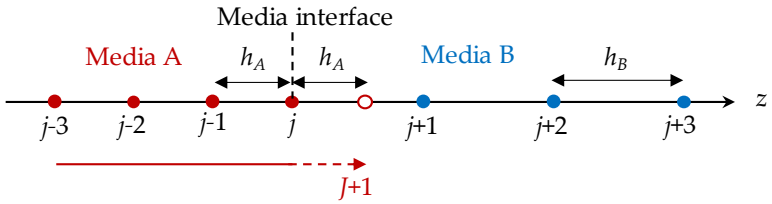

Figure 3. Schematic diagram of the MIB method addressing medium interface conditions.

Using the fourth-order finite difference scheme, the first derivatives at the upper and lower sides of the interface point can be, respectively, expressed as:

$$\left(\frac{\partial \hat{p}}{\partial z}\right)_{j^-} = \frac{-\hat{p}_{j-3} + 6\hat{p}_{j-2} - 18\hat{p}_{j-1} + 10\hat{p}_j + 3q_{J+1}}{12h} \tag{39}$$

$$\left(\frac{\partial \hat{p}}{\partial z}\right)_{j^+} = \frac{-25\hat{p}_j + 48\hat{p}_{j+1} - 36\hat{p}_{j+2} + 16\hat{p}_{j+3} - 3\hat{p}_{j+4}}{12h} \tag{40}$$

Then, according to the continuity condition of the vertical velocity ($\frac{1}{\rho_A}\left(\frac{\partial \hat{p}}{\partial z}\right)_{j^-} = \frac{1}{\rho_B}\left(\frac{\partial \hat{p}}{\partial z}\right)_{j^+}$), one can obtain

$$\begin{aligned} q_{J+1} = \; & \tfrac{1}{3}\Big[\rho_A\rho_B^{-1}\left(-25\hat{p}_j + 48\hat{p}_{j+1} - 36\hat{p}_{j+2} + 16\hat{p}_{j+3} - 3\hat{p}_{j+4}\right) \\ & -\left(-\hat{p}_{j-3} + 6\hat{p}_{j-2} - 18\hat{p}_{j-1} + 10\hat{p}_j\right)\Big] \end{aligned} \tag{41}$$

For the lower side of the interface, the point j (and its value $\hat{p}_j$) can be considered as the "upper boundary", and thus the boundary scheme can be used to calculate the second derivative at point j + 1. In this study, media B refers to the sediment, and thus the standard second-order accuracy three-point central difference scheme is used to calculate the second derivative at the point j+1.

For the upper side of the interface (media A, referring to the water here), the second derivative at point j is discretized using the fourth-order finite difference scheme, expressed as:

$$\begin{aligned} \frac{\partial}{\partial z}\left(\frac{\partial \hat{p}}{\partial z}\right)\Big|_j = \; & \tfrac{1}{120h}\Big[-3\left(\tfrac{\partial \hat{p}}{\partial z}\right)_{j-5/2} + 25\left(\tfrac{\partial \hat{p}}{\partial z}\right)_{j-3/2} - 225\left(\tfrac{\partial \hat{p}}{\partial z}\right)_{j-1/2} \\ & +128\left(\tfrac{\partial \hat{p}}{\partial z}\right)_{j^-} + 75\left(\tfrac{\partial \hat{p}}{\partial z}\right)_{(j+1/2)^-}\Big] \end{aligned} \tag{42}$$

where $\left(\frac{\partial \hat{p}}{\partial z}\right)_{j^-}$ is calculated using Equation (39), and $\left(\frac{\partial \hat{p}}{\partial z}\right)_{(j+1/2)^-}$ is discretized using a difference scheme similar to Equation (37):

$$\left(\frac{\partial \hat{p}}{\partial z}\right)_{(j+1/2)^-} = \frac{1}{24h}\left(22q_{J+1} - 17\hat{p}_j - 9\hat{p}_{j-1} + 5\hat{p}_{j-2} - \hat{p}_{j-3}\right) \tag{43}$$

The first derivatives at other half-integer index points are calculated using a fourth-order accurate interior point scheme. Moreover, second derivatives at points above the point j can be discretized using the interior point scheme.

3.3. Source Treatment Method

According to the definition of the Dirac function $\delta(x)$, it has the following properties: (1) it takes infinity at x = 0 and 0 at other positions; (2) the integral is 1 in the range containing x = 0 and 0 otherwise. There are various treatments of the Dirac function, and an approximation commonly seen in finite difference models is taken here, which is also used by the FEM in the SPARC program.

As shown in Figure 4, if the source point is located between the grid points js and js + 1 ($z_{js} < z_s \leq z_{js+1}$), and the distance between these two points is h_s, then the Dirac function is approximated linearly as:

$$\delta(z - z_s) \approx \delta^{FD}(z - z_s) = \begin{cases} (1 - w_s)/h_s, & if\ z \in (z_{js} - h_s/2,\ z_{js} + h_s/2) \\ w_s/h_s & ,if\ z \in (z_{js+1} - h_s/2,\ z_{js+1} + h_s/2) \\ 0 & , \quad otherwise \end{cases} \tag{44}$$

where $w_s < (z_s - z_{js})/h_s$. This approximation will keep the value of the integral unchanged at 1, i.e.,

$$\int_0^H \delta(z - z_s)dz \approx \int_{z_{js} - h_s/2}^{z_{js} + h_s/2} \frac{1 - w_s}{h_s} dz + \int_{z_{js+1} - h_s/2}^{z_{js+1} + h_s/2} \frac{w_s}{h_s} dz = 1 - w_s + w_s = 1 \tag{45}$$

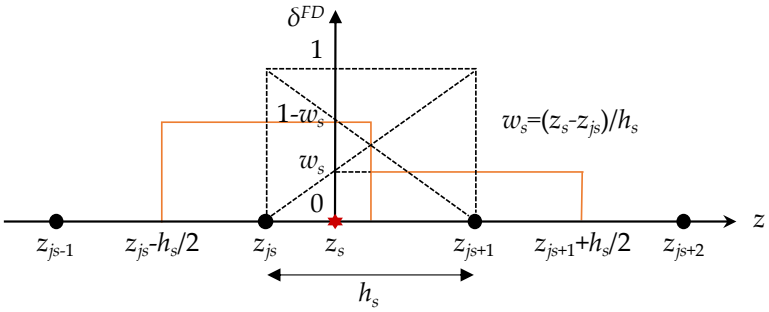

Figure 4. Schematic diagram of the source treatment method.

After adopting the Dirac approximation function, the Equation (26) reduces to:

$$RHS_{4\text{th}} = -2s(t)\delta^{FD}(z - z_s) + \frac{\hat{p}^{(n-1)} - 2\hat{p}^{(n)}}{(c\Delta t)^2} + \frac{d(z)}{2\Delta t}\mathcal{L}_{4th}\left(\hat{p}^{(n-1)}\right) - \mathcal{L}_{4th}\left(\hat{p}^{(n)}\right) \tag{46}$$

where $s(t)$ uses a single sine pulse in this paper:

$$S(t) = \begin{cases} \sin(\omega t), & 0 \leq t \leq \frac{1}{f} \\ 0, & otherwise \end{cases} \tag{47}$$

It should be noted that the main difference between this work and our previous efforts [24] lies in the contrast between the frequency and time domains. In the frequency domain, the kernel function must be solved iteratively by constructing a complex system of equations. However, the time-stepping method used in the time domain does not require this. Additionally, although this paper also utilizes the similar fourth-order FDM at interior points, the FD schemes are not the same at the boundary and source points. In particular, at the sound source, the MIB scheme is not used in this work, but the Dirac function approximation is used instead.

4. Test Cases

Herein, the time-marched wavenumber integration model SPARC has been improved by replacing the original second-order FEM with the proposed fourth-order FDM for solving the depth equation in the time domain. For ease of description, the original SPARC

program will be referred to as the FEM program, while our improved program will be referred to as the FDM program.

To verify the accuracy and performance of the FEM and FDM programs for solving the transient ocean acoustic field excited by a pulse source, three tests were performed: Lloyd's mirror, the ideal waveguide, and the head wave. The water parameters are homogeneous in all cases, with a density of 1000 kg/m^3, a sound speed of 1500 m/s, and no absorption. The Lloyd's mirror and the ideal waveguide cases can be solved analytically using the image method, and thus they allow accuracy verification of both programs in calculating the acoustic field in a semi-infinite space and a single-layer ocean environment, respectively. The head wave case involves a layered marine environment with upper and lower lossless liquid half-spaces. In this case, the comparison is limited to the consistency and the runtime of the two programs, as there is no exact reference solution available.

4.1. Lloyd's Mirror

The Lloyd's mirror case is a semi-infinite space problem with a source depth of 30 m, a source frequency of f = 50 Hz, and a receiver depth of 150 m. The top of the water layer is a pressure release boundary, and the bottom of the water layer is infinitely deep. According to the image method, the analytical sound pressure in the Lloyd's mirror case is given by:

$$p(r,z,t) = \frac{s(t-R_1/c)}{R_1} - \frac{s(t-R_2/c)}{R_2} \tag{48}$$

where $R_1 = \sqrt{r^2+(z-z_s)^2}$ and $R_2 = \sqrt{r^2+(z+z_s)^2}$.

Figure 5 shows the temporal acoustic field snapshots at t = 0.3 s computed by the FEM and FDM programs compared to the analytical solution, respectively. The FEM program uses a vertical grid resolution of PPW = 20, while the FDM program uses PPW = 20 and 15. Both programs produce the correct sound pressure field, which is similar to the analytical solution. However, it can be observed that the FEM results are not as accurate as the FDM results. The sound field of the FDM with PPW = 15 is slightly inferior to that of the FDM with PPW = 20, but still superior to that of the FEM (PPW = 20).

Since this case has an analytical solution, it is possible to calculate the root mean square error of the sound pressure for both programs, using the following formula:

$$Error = \sqrt{\frac{1}{n}\sum_{i=1}^{n}\left(p_i^{Num}-p_i^{Exact}\right)^2} \tag{49}$$

where p_i^{Num} is the numerical solution of the pressure at the grid point i, p_i^{Exact} is the analytical solution, and n is the total number of grid points. Figure 6 presents the error versus time curves obtained from both programs. It can be observed that the FDM program with PPW = 15 has a smaller error than the FEM program with PPW = 20.

Figure 7 shows the sound pressure versus time curves at the receiver point (r = 50 m, z = 150 m) obtained from the analytical formula and the solutions computed by both programs. It can be seen that the three curves generally agree, confirming the accuracy of both programs. In addition, the first wave crest of the pulse arriving at the receiver point is amplified, and it is evident that the FDM program with PPW = 15 achieves a higher level of accuracy than the FEM program with PPW = 20.

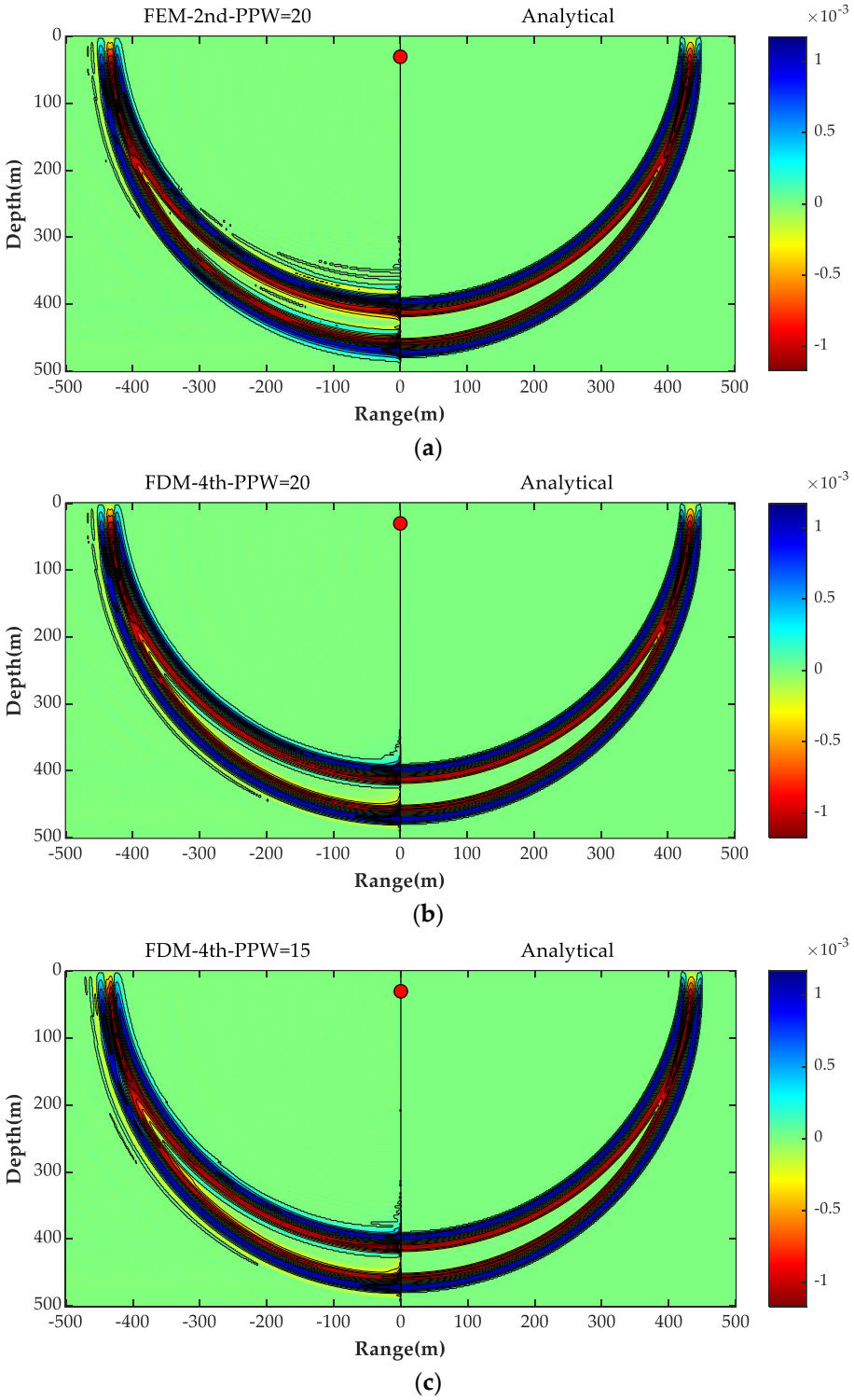

Figure 5. Comparison of sound pressure snapshots for the Lloyd's mirror case at t = 0.3 s: (**a**) FEM-*PPW* = 20, (**b**) FDM-*PPW* = 20, and (**c**) FDM-*PPW* = 15 vs. analytical solution.

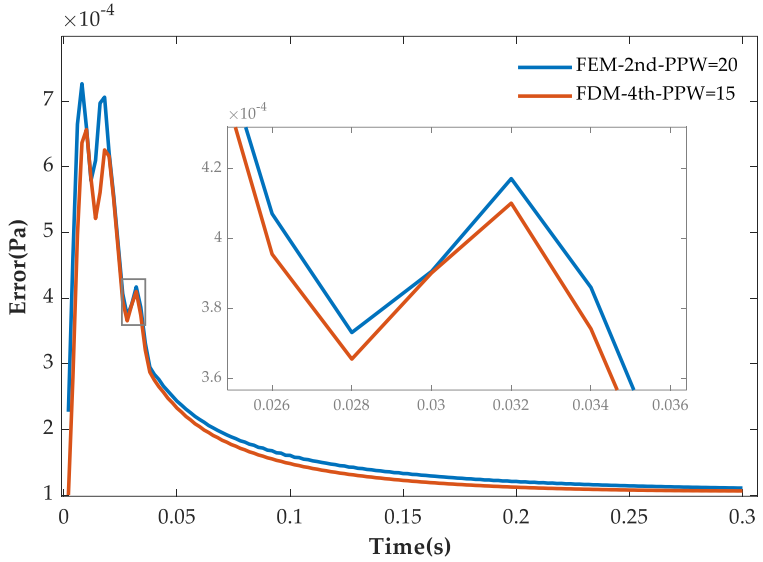

Figure 6. Root mean square error vs. time curves for the Lloyd's mirror case.

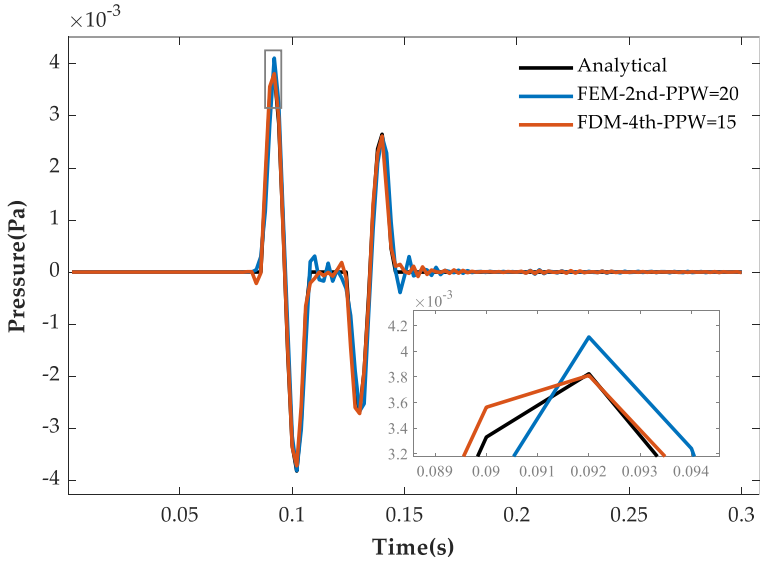

Figure 7. Pressure vs. time curves at the receiver point (r = 50 m, z = 150 m) for the Lloyd's mirror case.

4.2. Ideal Waveguide

The ideal waveguide is a single-layer fluid waveguide problem, and the upper and lower surfaces of the water layer are both pressure release boundaries. Herein, the source frequency is f = 50 Hz, and the depths of the water layer, the sound source, and the receiver are 90 m, 30 m, and 60 m, respectively. According to the image method, the analytical sound pressure in the ideal waveguide is given by:

$$p(r,z,t) = \sum_{m=1}^{\infty}\left[\frac{s(t-R_{m1}/c)}{R_{m1}} - \frac{s(t-R_{m2}/c)}{R_{m2}} - \frac{s(t-R_{m3}/c)}{R_{m3}} + \frac{s(t-R_{m4}/c)}{R_{m4}}\right] \quad (50)$$

where

$$R_{mn} = \sqrt{r^2 + \Delta z_{mn}^2},\ \Delta z_{mn}^2 = (z - z_{mn})^2,\ n = 1,2,3,4 \quad (51)$$

and $z_{m1} = 2(m-1)D + z_s$, $z_{m2} = 2mD - z_s$, $z_{m3} = -z_{m1}$, $z_{m4} = -z_{m2}$. Figure 8 shows the temporal acoustic field snapshots at t = 0.3s computed by the FEM and FDM programs compared to the analytical solution, respectively. The FEM program uses a vertical grid resolution of PPW = 20, while the FDM program uses PPW = 20 and 15. It is clear that

the results obtained by the FEM program have a relatively large error compared to the analytical solution. In contrast, the solution of the FDM program closely matches the analytical solution, even with fewer grid points (*PPW* = 15).

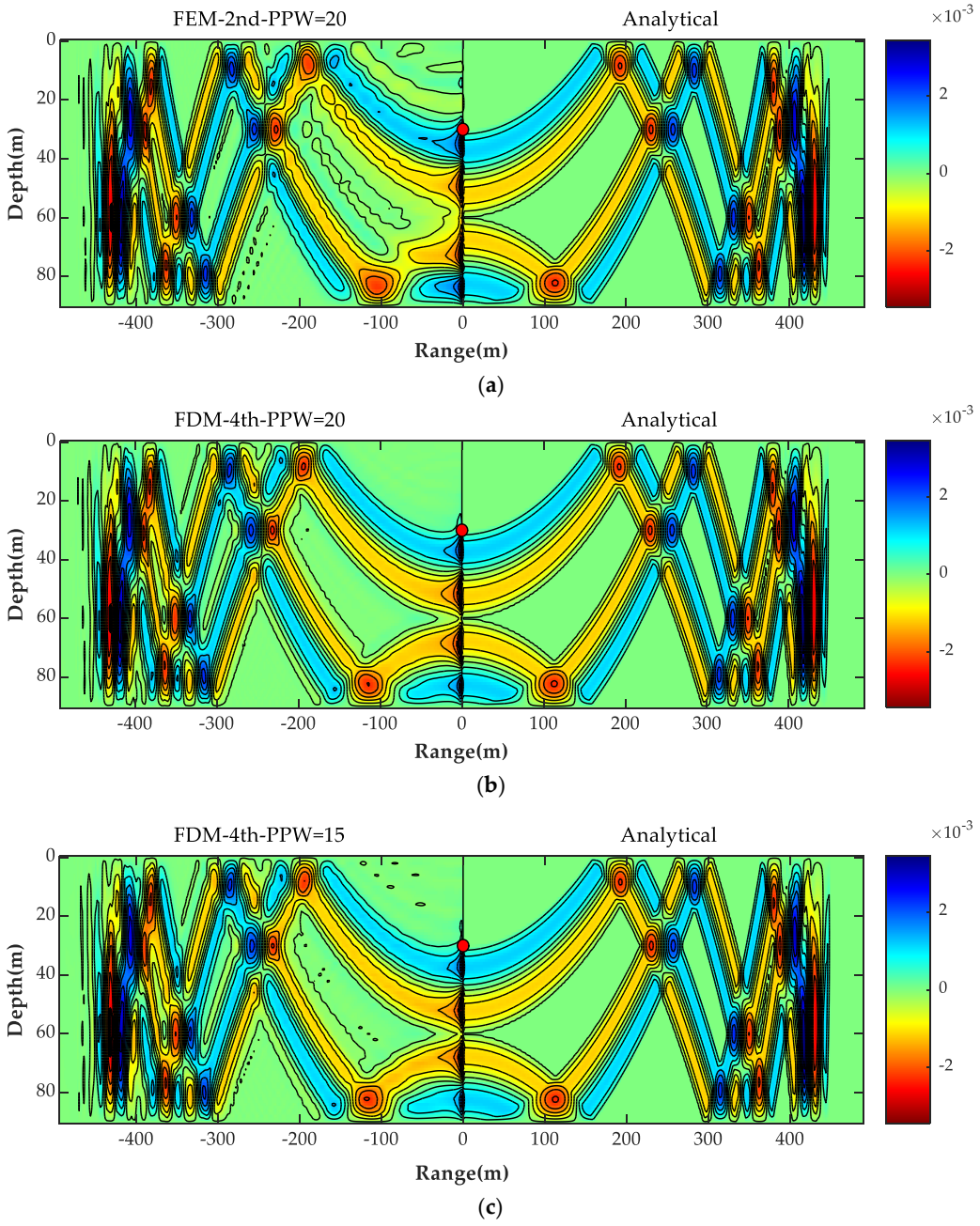

Figure 8. Comparison of sound pressure snapshots for the ideal waveguide case at t = 0.3 s: (**a**) FEM-*PPW* = 20, (**b**) FDM-*PPW* = 20, and (**c**) FDM-*PPW* = 15 vs. analytical solution.

Figure 9 displays the root mean square error versus time curves obtained from both programs. It can be seen that the FDM program with *PPW* = 15 has a smaller error than the FEM program with *PPW* = 20, which is consistent with the Lloyd's mirror case.

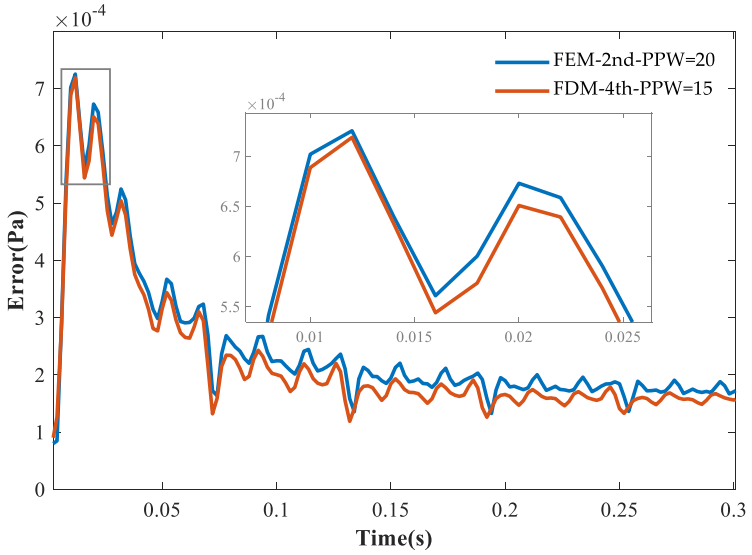

Figure 9. Root mean square error vs. time curves for the ideal waveguide case.

Figure 10 shows the sound pressure versus time curves at the receiver point (r = 100 m, z = 60 m) obtained from the analytical formula and the solutions computed by the FEM and FDM programs. It can be observed that the three curves are in general agreement, and the FDM achieves a higher level of accuracy compared to the FEM, even with fewer grid points.

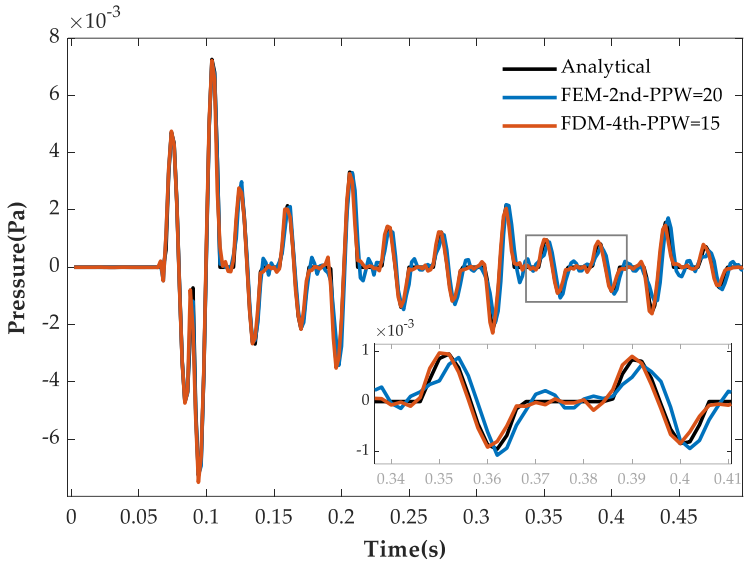

Figure 10. Pressure vs. time curves at the receiver point (r = 100 m and z = 60 m) for the ideal waveguide case.

4.3. Head Wave

The head wave problem [20] is a layered environment consisting of two lossless fluid half-spaces. Both half-spaces have the same density of 1000 kg/m^3, but their sound speeds are different, 1500 m/s and 2500 m/s, respectively. The coordinate origin is set at a point 30 m above the source, the sound source frequency is 50 Hz, and the interface between the two half-spaces is located at a depth of 90 m.

Figure 11 shows the temporal acoustic field snapshots at t = 0.12 s computed by the FEM and FDM programs. The FEM program uses a vertical grid resolution of PPW = 20, while the FDM program uses PPW = 15. It can be observed that although the FDM uses fewer grid points, the results obtained by both methods are generally consistent.

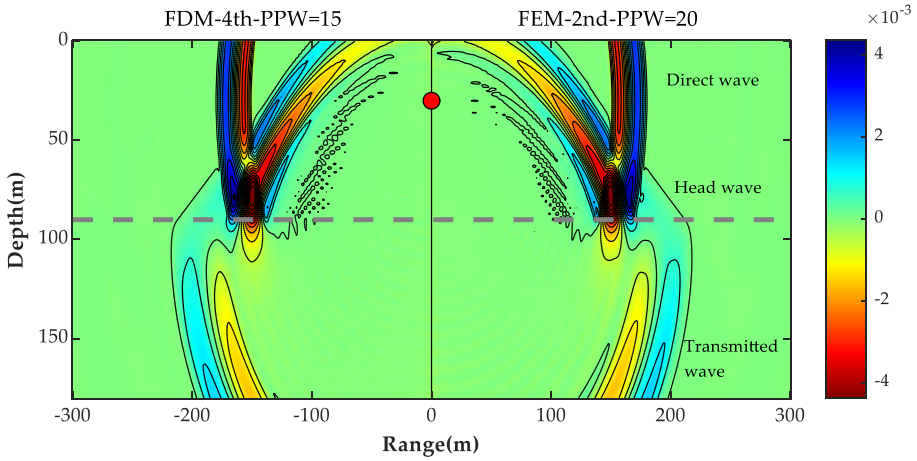

Figure 11. Comparison of sound pressure snapshots for the head wave case at t = 0.12 s.

Figure 12 presents the sound pressure versus time curves at the receiver point (r = 50 m, z = 50 m) computed by the FEM and FDM programs. It shows that the results obtained by the two programs are in good agreement. Additionally, the FDM program uses a smaller *PPW* value than the FEM program, indicating that the FDM requires fewer grid points to achieve the same level of accuracy as the FEM.

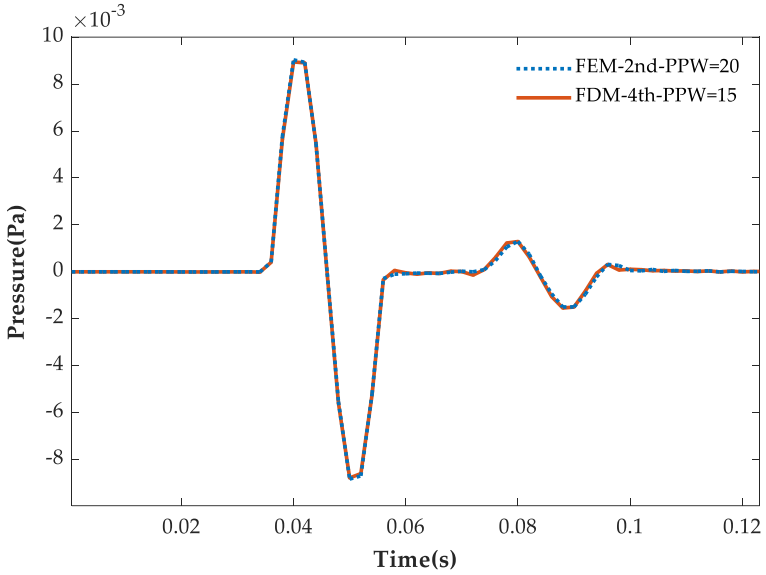

Figure 12. Pressure vs. time curves at the receiver point (r = 50 m and z = 50 m) for the head wave case.

4.4. Computation Analysis

Since the fourth-order FDM method is based on five points for computation, while the second-order FEM method only uses three points, it is important to analyze the computational effort required for each method. To illustrate the difference in computational cost between the improved program and the original program, a comparison is made below in terms of both the number of floating-point operations and the running time.

By comparing the FEM and FDM programs, the main difference between the floating-point operations produced during the computation is in the time-stepping solution part. Since there are relatively few calculations at boundary and sound–source interfaces, only the interior point scheme is considered for the analysis. In the FEM program, the time-stepping solver involves six multiplication operations and five addition operations per

iteration. The pseudocode for the *RHS* computation in the FEM program is shown in Table 1.

Table 1. The *RHS* computation at interior points in the FEM program.

```
Do j = 2, N_Tot1 − 1! The number of interior points
    U2(j) = AD1(j) * U1(j) + AE1(j) * U1(j − 1) + AE1(j + 1) * U1(j + 1) +
            AD0(j) * U0(j) + AE0(j) * U0(j − 1) + AE0(j + 1) * U0(j + 1)
End do
! U0 denotes the kernel function at the previous time step
! U1 denotes the kernel function at the current time step
! U2 denotes the right-hand side
! AD0 denotes the diagonal element of the previous time step coefficient matrix
! AE0 denotes the off-diagonal element of the previous time step coefficient matrix
! AD1 denotes the diagonal element of the current time step coefficient matrix
! AE1 denotes the off-diagonal element of the current time step coefficient matrix
```

In the FDM program, the interior point scheme from Equations (33) and (34) can be simplified by extracting and saving the common factor $(1/24/h)^2$ as a coefficient. And then, the calculation of its right-hand side can be simplified as:

$$RHS_{4\text{th}} = Q_1 * \hat{p}^{(n-1)} + Q_2 * \frac{\partial}{\partial z}\left(\frac{\partial \hat{p}^{(n-1)}}{\partial z}\right) + Q_3 * \hat{p}^{(n)} + Q_4 * \frac{\partial}{\partial z}\left(\frac{\partial \hat{p}^{(n)}}{\partial z}\right) \tag{52}$$

where Q_1, Q_2, Q_3, and Q_4 are coefficients that have been pre-calculated (Q_2 and Q_4 both have the factor $(1/24/h)^2$). Therefore, the FDM program requires six multiplication operations and nine addition operations per iteration. In this paper, since only the non-absorbing marine environment is being considered, both methods are solved explicitly, adding one multiplication operation to each iteration. The total number of operations for both methods can be calculated as follows:

$$\begin{aligned} Mul.ops(FEM_{PPW=20}) &= 7N_{step}N_{kr}N_{Tot1} \\ Add.ops(FEM_{PPW=20}) &= 5N_{step}N_{kr}N_{Tot1} \end{aligned} \tag{53}$$

$$\begin{aligned} Mul.ops(FDM_{PPW=20}) &= 7N_{step}N_{kr}N_{Tot1} \\ Add.ops(FDM_{PPW=20}) &= 9N_{step}N_{kr}N_{Tot1} \end{aligned} \tag{54}$$

where N_{step} represents the total number of time steps, N_{kr} is the number of horizontal wavenumbers considered in the integration process, and N_{Tot1} is the total number of points in the depth direction. These values can be further expressed as follows (Δt has been defined by Equation (24)):

$$N_{step} = \frac{t_{\max}}{\Delta t} \approx \frac{t_{\max} c_{\max}}{CFL\lambda_{\min}} \tag{55}$$

$$N_{kr} = \frac{k_{\max} R_{\max}}{2\pi} \tag{56}$$

$$N_{Tot1} = \frac{H}{\Delta z_{\min}} + 1 \approx \frac{H}{\lambda_{\min}} PPW \tag{57}$$

When both *PPW*s are set to 20, each iteration of the fourth-order FDM requires four additional addition operations, resulting in a higher computational cost and longer computation time. However, if *PPW* = 15 is used in the fourth-order FDM, the operations will change to:

$$\begin{aligned} Mul.ops(FDM_{PPW=15}) &= 7N_{step}N_{kr}\left(\tfrac{15}{20}N_{Tot1}\right) = 5.25N_{step}N_{kr}N_{Tot1} \\ Add.ops(FDM_{PPW=15}) &= 9N_{step}N_{kr}\left(\tfrac{15}{20}N_{Tot1}\right) = 6.75N_{step}N_{kr}N_{Tot1} \end{aligned} \tag{58}$$

In general, the cost of a computer performing an addition operation is lower than performing a multiplication operation. When compared to the second-order FEM with *PPW* = 20, the fourth-order FDM with *PPW* = 15 reduces computational costs due to the reduction in the number of multiplication operations, despite having more addition operations.

Table 2 displays the running time of the test cases mentioned above, providing an efficiency comparison between the proposed FDM program and the original FEM program. Both programs are written in the Fortran language. The tests were conducted on a laptop computer equipped with an Intel i7-12700H CPU and 64 GB of memory, using a single-threaded process. The values listed in the table represent the average running time over 10 test runs. The results show that the FDM with *PPW* = 15 has a shorter running time compared to the FEM program while maintaining similar or even higher accuracy. This can be attributed to the fact that the fourth-order FDM has higher accuracy and better computational efficiency compared to the second-order FEM, allowing for a reduction in the number of vertical grid points.

Table 2. Running time of all cases.

Cases	FEM-2nd (*PPW* = 20)	FDM-4th (*PPW* = 20)	FDM-4th (*PPW* = 15)
Lloyd's mirror	16.310 s	19.547 s	14.120 s
Ideal waveguide	2.712 s	3.185 s	2.373 s
Head wave	20.116 s	24.506 s	17.336 s

5. Discussion

A high-order FDM has been proposed for solving the depth equation in the time-marched wavenumber integration model SPARC. This model is specifically designed to address the problem of pulse propagation in horizontally layered ocean environments. Three classic acoustic tests have demonstrated that the improved program, which utilizes the proposed fourth-order FDM, requires fewer grid points compared to the original SPARC program that uses the second-order FEM. Despite using fewer grid points, the improved program maintains the same level of accuracy, and in some cases, even better accuracy, resulting in lower computational costs and faster processing. The new model is consistent with the existing model in terms of its scope of application. This means that it can be used in the same situations as the current model. However, the present method has a greater advantage when dealing with large-scale transient sound field calculations or when multiple transient sound fields need to be calculated. Additionally, when there is no reference solution available for the sound field, the method described in this paper will provide a higher level of confidence.

This study aims to assist researchers in gaining a better understanding of how to address transient acoustic field problems in stratified marine environments. However, the wavenumber integration model SPARC is only suitable for horizontal seabed scenarios. To more accurately simulate the transient sound propagation in underwater environments, further research is needed on time-domain underwater acoustic models that can handle range-dependent seabeds. In the future, our work will focus on optimizing finite element procedures and implicit calculations, with consideration for attenuation. It is also crucial to conduct testing on a wider range of acoustic cases in order to ensure comprehensive results.

Author Contributions: Conceptualization, W.L. and G.X.; methodology, W.L. and X.X.; software, X.X.; validation, X.X. and W.L.; writing, X.X and W.L.; visualization, X.X.; funding acquisition, G.X. and W.L. All authors have read and agreed to the published version of the manuscript.

Funding: This work was supported in part by the National Key Research and Development Program of China (Grant No. 2022YFC3103404) and in part by the National Natural Science Foundation of China (Grant No. 61972406).

Institutional Review Board Statement: Not applicable.

Informed Consent Statement: Not applicable.

Data Availability Statement: Data are contained within the article.

Acknowledgments: The authors are grateful to M. Porter for providing the SPARC program [26].

Conflicts of Interest: The authors declare no conflicts of interest.

References

1. Jensen, F.B. Wave theory modelling: A convenient approach to CW and pulse propagation modelling in low-frequency acoustics. *IEEE J. Ocean. Eng.* **1988**, *13*, 186–197. [CrossRef]
2. Jensen, F.B.; Ferla, C.M.; Nielsen, P.L.; Martinelli, G. Broadband Signal Simulation in Shallow Water. *J. Comput. Acoust.* **2003**, *11*, 577–591. [CrossRef]
3. Jensen, F.B.; Kuperman, W.A.; Porter, M.B.; Schmidt, H.; Tolstoy, A. *Computational Ocean Acoustics*; Springer: Berlin/Heidelberg, Germany, 2011; Volume 2011.
4. Sertlek, H.O.; Aksoy, S. Benchmarking of acoustic pulse propagation problems in an isovelocity waveguide by an analytical time domain normal mode method. *Proc. Meet. Acoust.* **2013**, *17*, 070103. [CrossRef]
5. Skarsoulis, E.K. Second-Order Fourier Synthesis of Broadband Acoustic Signals Using Normal Modes. *J. Comput. Acoust.* **1997**, *05*, 355–370. [CrossRef]
6. Porter, M.B. Beam tracing for two- and three-dimensional problems in ocean acoustics. *J. Acoust. Soc. Am.* **2019**, *146*, 2016–2029. [CrossRef] [PubMed]
7. Tu, H.; Wang, Y.; Lan, Q.; Liu, W.; Xiao, W.; Ma, S. A Chebyshev-Tau spectral method for normal modes of underwater sound propagation with a layered marine environment. *J. Sound Vib.* **2021**, *492*, 115784. [CrossRef]
8. Schmidt, H.; Glattetre, J. A fast field model for three-dimensional wave propagation in stratified environments based on the global matrix method. *J. Acoust. Soc. Am.* **1985**, *78*, 2105–2114. [CrossRef]
9. Tu, H.; Wang, Y.; Zhang, Y.; Wang, X.; Liu, W. A spectrally discretized wide-angle parabolic equation model for simulating acoustic propagation in laterally inhomogeneous oceans. *J. Acoust. Soc. Am.* **2023**, *153*, 3334. [CrossRef] [PubMed]
10. Lee, B.M.; Dowling, D.R. Tangent linear approximations for split-step Padé solutions of the parabolic-equation method in two dimensions. *J. Acoust. Soc. Am.* **2023**, *154*, A180. [CrossRef]
11. Zingarelli, R.A.; Chin-Bing, S.A.; Collins, M.D. Optimizations for Fourier synthesized time domain pulse propagation calculations. In Proceedings of the OCEANS 2009, Biloxi, MS, USA, 26–29 October 2009; pp. 1–5.
12. Deavenport, R.L.; Gilchrest, M.J.; Thomson, D.J. Acoustic modelling of a transient source in shallow water. *Appl. Acoust.* **2019**, *150*, 227–235. [CrossRef]
13. An, L.; Qiu, Y.; Wang, X.; Zhang, L.; Huang, R. Low resolution fourier synthesis modelling for underwater acoustic channel impulse response. *Appl. Acoust.* **2022**, *188*, 108596. [CrossRef]
14. Murphy, J.E. Finite-difference treatment of a time-domain parabolic equation: Theory. *J. Acoust. Soc. Am.* **1985**, *77*, 1958–1960. [CrossRef]
15. Collins, M.D. The time-domain solution of the wide-angle parabolic equation including the effects of sediment dispersion. *J. Acoust. Soc. Am.* **1988**, *84*, 2114–2125. [CrossRef]
16. Özkan Sertlek, H. Time domain normal mode analysis of underwater acoustic wave propagation for a single layered acoustic channel in two dimensional Cartesian coordinates. *J. Acoust. Soc. Am.* **2009**, *126*, 3373. [CrossRef]
17. Cristini, P.; Komatitsch, D. Some illustrative examples of the use of a spectral-element method in ocean acoustics. *J. Acoust. Soc. Am.* **2012**, *131*, EL229–EL235. [CrossRef] [PubMed]
18. Plotnick, D.; Marston, P.L. Modeling and experimental validation of an evanescent wavefield using a wavenumber integration method. *J. Acoust. Soc. Am.* **2016**, *139*, 1986. [CrossRef]
19. Etter, P.C. *Underwater Acoustic Modeling and Simulation*, 5th ed.; CRC Press: Boca Raton, FL, USA, 2018; p. 608.
20. Porter, M.B. The time-marched fast-field program (FFP) for modeling acoustic pulse propagation. *J. Acoust. Soc. Am.* **1990**, *87*, 2013–2023. [CrossRef]
21. Isakson, M.J.; Yarbrough, R.A.; Wilson, P.S. Finite-element modeling of long range, range-dependent acoustic propagation in shallow water. *J. Acoust. Soc. Am.* **2007**, *122*, 3074. [CrossRef]
22. Zhou, Y.C.; Wei, G.W. On the fictitious-domain and interpolation formulations of the matched interface and boundary (MIB) method. *J. Comput. Phys.* **2006**, *219*, 228–246. [CrossRef]
23. Pan, K.; Tan, Y.; Hu, H. An interpolation matched interface and boundary method for elliptic interface problems. *J. Comput. Appl. Math.* **2010**, *234*, 73–94. [CrossRef]
24. Liu, W.; Zhang, L.; Wang, Y.; Cheng, X.; Xiao, W. A Vector Wavenumber Integration Model of Underwater Acoustic Propagation Based on the Matched Interface and Boundary Method. *J. Mar. Sci. Eng.* **2021**, *9*, 1134. [CrossRef]

25. Liu, W.; Xu, G.; Cheng, X.; Wang, Y. A Novel Finite Difference Scheme for Normal Mode Models in Underwater Acoustics. *J. Mar. Sci. Eng.* **2023**, *11*, 553. [CrossRef]
26. Porter, M.B. Acoustics Toolbox. 2023. Available online: http://oalib.hlsresearch.com/AcousticsToolbox/ (accessed on 25 April 2024).